

**Manuscript version: Author's Accepted Manuscript**

The version presented in WRAP is the author's accepted manuscript and may differ from the published version or Version of Record.

**Persistent WRAP URL:**

<http://wrap.warwick.ac.uk/123458>

**How to cite:**

Please refer to published version for the most recent bibliographic citation information. If a published version is known of, the repository item page linked to above, will contain details on accessing it.

**Copyright and reuse:**

The Warwick Research Archive Portal (WRAP) makes this work by researchers of the University of Warwick available open access under the following conditions.

Copyright © and all moral rights to the version of the paper presented here belong to the individual author(s) and/or other copyright owners. To the extent reasonable and practicable the material made available in WRAP has been checked for eligibility before being made available.

Copies of full items can be used for personal research or study, educational, or not-for-profit purposes without prior permission or charge. Provided that the authors, title and full bibliographic details are credited, a hyperlink and/or URL is given for the original metadata page and the content is not changed in any way.

**Publisher's statement:**

Please refer to the repository item page, publisher's statement section, for further information.

For more information, please contact the WRAP Team at: [wrap@warwick.ac.uk](mailto:wrap@warwick.ac.uk).

# Visualizing electrostatic gating effects in two-dimensional heterostructures

Paul V Nguyen,<sup>1</sup> Natalie C Teutsch\*,<sup>2</sup> Nathan Wilson,<sup>1</sup> Joshua Kahn,<sup>1</sup> Xue Xia\*,<sup>2</sup> Abigail J Graham\*,<sup>2</sup> Viktor Kandyba,<sup>3</sup> Alessio Giampietri,<sup>3</sup> Alexei Barinov,<sup>3</sup> Gabriel C Constantinescu,<sup>4</sup> Nelson Yeung,<sup>2</sup> Nicholas D M Hine,<sup>2</sup> Xiaodong Xu,<sup>1,5\*</sup> David H Cobden,<sup>1\*</sup> Neil R Wilson\*<sup>2\*</sup>

<sup>1</sup>Department of Physics, University of Washington, Seattle, Washington 98195, USA

<sup>2</sup>Department of Physics, University of Warwick, Coventry, CV4 7AL, UK

<sup>3</sup>Elettra - Sincrotrone Trieste, S.C.p.A., Basovizza (TS), 34149, Italy

<sup>4</sup>TCM Group, Cavendish Laboratory, University of Cambridge, 19 JJ Thomson Avenue, Cambridge CB3 0HE, UK

<sup>5</sup>Department of Material Science and Engineering, University of Washington, Seattle, Washington 98195, USA

Submitted and accepted to Nature

**The ability to directly monitor the states of electrons in modern field-effect devices, for example imaging local changes in the electrical potential, Fermi level and band structure as a gate voltage is applied, could transform understanding of the device physics and function. Here we show that submicrometre angle-resolved photoemission spectroscopy<sup>1–3</sup> ( $\mu$ -ARPES) applied to two-dimensional van der Waals heterostructures<sup>4</sup> affords this ability. In two-terminal graphene devices we observe a shift of the Fermi level across the Dirac point, with no detectable change in the dispersion, as a gate voltage is applied. In two-dimensional semiconductor devices we see the conduction band edge appear as electrons accumulate, thereby firmly establishing its energy and momentum. In the case of monolayer WSe<sub>2</sub> we observe that the band gap is renormalized downwards by several hundred meV, approaching the exciton energy, as the electrostatic doping increases. Both optical spectroscopy and  $\mu$ -ARPES can be carried out on a single device, allowing definitive studies of the relationship between gate-controlled electronic and optical properties. The technique provides a powerful new means to study not only fundamental semiconductor physics but also intriguing phenomena such as topological transitions<sup>5</sup> and many-body spectral reconstructions under electrical control.**

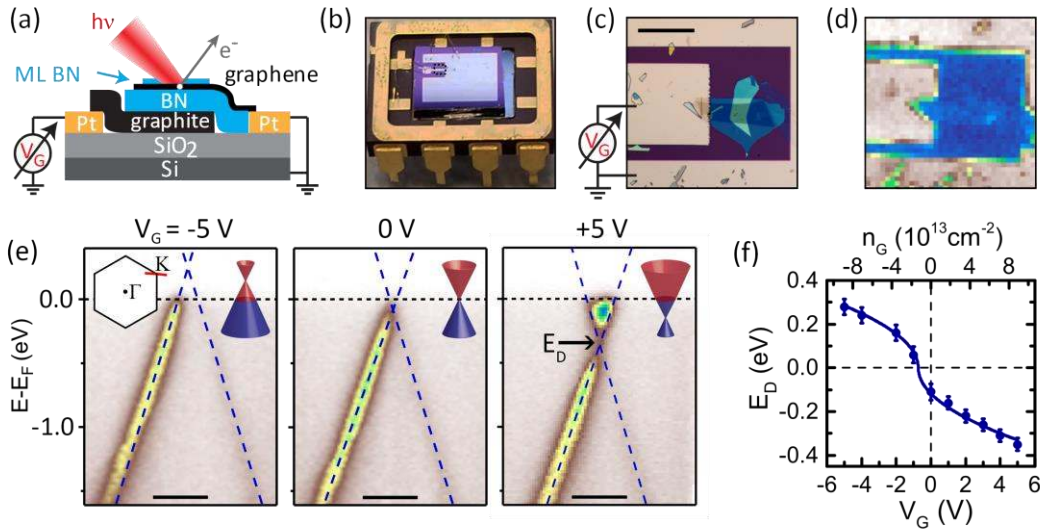
In ARPES one measures the distribution of energy and momentum of electrons photoemitted from a solid sample subjected to a narrow-spectrum ultraviolet or X-ray excitation. This provides information about the energy and momentum of the initial occupied electron states, and hence the band structure and Fermi level. As electrons are emitted only from very near the sample surface, ARPES is not useful for studying conventional semiconductor devices. On the other hand, it is well suited to probing two-dimensional (2D) materials, and has been applied to films of graphene<sup>6</sup>, transition metal dichalcogenides (MX<sub>2</sub>, where M=Mo,W,Ta etc and X=S,Se,Te)<sup>7,8</sup>, and others<sup>9,10</sup>. While the excitation spot size is typically measured in millimetres, efforts have been made in the last decade<sup>2</sup> to perform ARPES with a focused beam suitable for small or nonuniform samples. Micrometre-scale spot sizes (hence  $\mu$ -ARPES) have been achieved in at least four commissioned synchrotron beamlines using Schwarzschild objectives<sup>1</sup>, Fresnel zone plates<sup>2,3</sup>, or capillary mirror optics<sup>11</sup>.  $\mu$ -ARPES has allowed the study of atomically thin exfoliated flakes of 2D materials, which are typically tens of microns or less in size<sup>12</sup>, and of heterostructures<sup>4</sup> made by stacking such flakes of different materials<sup>13,14</sup>, revealing for example band offsets and interlayer hybridization<sup>15–17</sup>. Such 2D heterostructures can be made into electrical and optical devices<sup>18</sup> by incorporating metal electrodes, opening up the possibility of using  $\mu$ -ARPES to monitor electronic structure in operating devices.

A major limitation of ARPES is that it probes only occupied electron states. A semiconductor sample must therefore be electron-doped in order to obtain a signal from the conduction band. Doping is usually achieved by depositing electropositive atoms such as alkali metals<sup>6–8,13</sup> on the surface. This

1 process cannot be controlled accurately and can only be reversed by high temperature annealing;  
 2 moreover, it chemically perturbs the electronic structure and introduces disorder through the random  
 3 distribution of dopants. In this work we demonstrate purely electrostatic doping, which has none of  
 4 these disadvantages. We thereby obtain momentum-resolved electronic spectra and direct  
 5 visualization of Fermi level shifts and band structure changes induced by applying a gate voltage.

6 We first demonstrate and validate the technique using graphene, then go on to apply it to the 2D  
 7  $\text{MX}_2$  semiconductors which are of interest for valleytronics and other applications<sup>18,19</sup>. Although it is  
 8 widely believed that all monolayer  $\text{MX}_2$  semiconductors have a direct band gap at the corner of the  
 9 hexagonal Brillouin zone,  $\mathbf{K}$ , the location of the conduction band edge (CBE) is not known with  
 10 certainty. This is illustrated by the wide range of reported band gap values for monolayer  $\text{WSe}_2$ , from  
 11 1.4 to 2.2 eV<sup>8,20–24</sup>. Also unclear is when the local conduction band minimum at the lower-symmetry  
 12 point  $\mathbf{Q}$  comes into play<sup>21,25</sup>. Using electrostatic doping in  $\mu$ -ARPES, we confirm that the CBE is at  $\mathbf{K}$  in  
 13 all the monolayer semiconductors,  $\text{MoS}_2$ ,  $\text{MoSe}_2$ ,  $\text{WS}_2$  and  $\text{WSe}_2$ , and in each case we obtain a measure  
 14 of the band gap. We also study the layer-number dependence in  $\text{WSe}_2$ , finding that the CBE moves to  
 15  $\mathbf{Q}$  in the bilayer, and measure for the first time the renormalization of the band structure on gating.  
 16

### 17 1. Electrostatic doping of graphene



18  
 19 **Figure 1. Visualizing electrostatic gating of monolayer graphene.** (a) Schematic of a 2D  
 20 heterostructure device with a stack comprising graphene encapsulated by BN on a graphite back gate.  
 21 Photoemission is measured with a focused micron-size X-ray beam spot (see Methods). The graphene  
 22 is grounded while a gate voltage  $V_G$  is applied to the gate. (b) Optical image of a device mounted in a  
 23 standard dual in-line package. (c) Optical zoom on the dotted box in (b) showing the stack, and (d)  
 24 scanning photoemission microscopy (SPEM) image of the same area (scale bar, 50  $\mu\text{m}$ ). (e) Energy-  
 25 momentum slices near the graphene  $\mathbf{K}$ -point, along the red line in the inset Brillouin zone, at the  
 26 labelled gate voltages. The dashed lines are linear dispersion fits; the Dirac point energy  $E_D$  is deduced  
 27 from their crossing point (scale bars, 0.2  $\text{\AA}^{-1}$ ). (f) Gate dependence of  $E_D$ , with error bars obtained from  
 28 the fitting procedure. The solid line is a fit based on the dispersion of graphene, with the gate-induced  
 29 electron density  $n_G$  shown on the top axis calculated from the capacitance (see Methods).  
 30

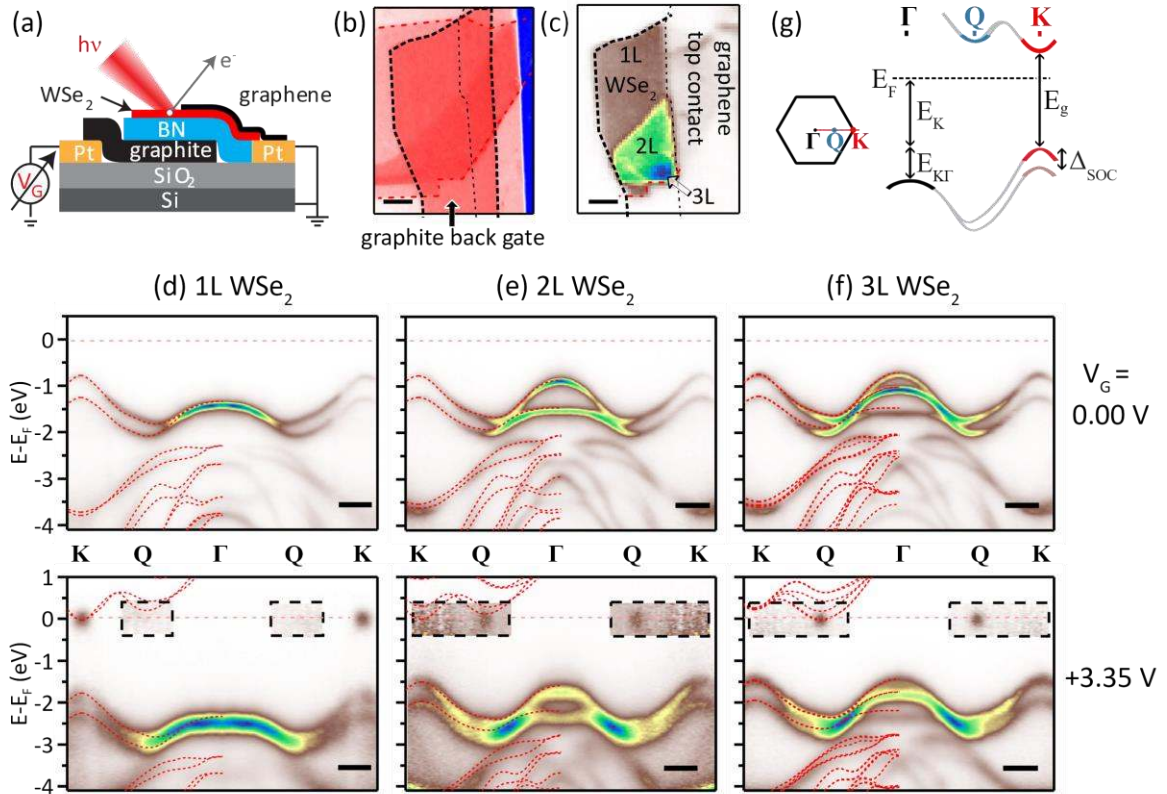
31 We first demonstrate gate-doping of monolayer graphene. A graphene sheet is capped by  
 32 monolayer hexagonal boron nitride (BN), supported on a BN flake over a graphite gate (Fig. 1a), and  
 33 located in a gap between two platinum electrodes on an  $\text{SiO}_2/\text{Si}$  substrate chip (Figs. 1b and 1c; see  
 34 Methods). A similar structure with two contacts to the graphene would function as a high-mobility  
 35 transistor<sup>26</sup>. Scanning photoemission microscopy (SPEM) is used to locate the sample in the ARPES  
 36 chamber (Fig. 1d; see Methods). Fig. 1e shows energy,  $E - E_F$ , vs momentum for a slice through the  
 37 Dirac cone near the graphene zone corner  $\mathbf{K}$ , acquired at a series of gate voltages  $V_G$  at 105 K. As  
 38 expected, the Dirac point energy  $E_D$  shifts from above the Fermi level  $E_F$  at  $V_G = -5$  V to below  $E_F$  at

1 +5 V. Fitting a linear dispersion,  $E(\mathbf{k}) = E_D \pm \hbar v_F k$  (dashed lines), gives  $E_D$  and the Fermi velocity  $v_F$ .  
 2 We find  $v_F = (9.3 \pm 0.1) \times 10^5 \text{ ms}^{-1}$  at  $V_G = 0 \text{ V}$ , with a weak  $V_G$  dependence (see Extended Data).  
 3 The variation of  $E_D$  with  $V_G$  (Fig. 1f) is consistent with the expected form for this dispersion (solid line, see Methods). No modification of the dispersion near  $E_D$ , which could arise due to interactions, is  
 4 detectable with the current spectral resolution.  
 5

6 The consistency of the above properties with the graphene literature, together with the  
 7 observation that the spectrum is undistorted as  $V_G$  is changed, implies that the photoelectron  
 8 trajectories are not affected by stray electric fields due to the gate voltage or charging effects. We  
 9 conclude that the technique produces accurate local electronic spectra during live electrostatic gating.  
 10

## 11 2. Electrostatic population of the conduction band in 2D semiconductors

12 An  $\text{MX}_2$  flake can be incorporated in the stack on top of the BN, partially overlapping graphene that  
 13 acts as a contact to it (Fig. 2a). Figures 2b and c are optical and SPEM images of a device with a  $\text{WSe}_2$   
 14 flake that has monolayer (1L), bilayer (2L) and trilayer (3L) regions. Figures 2d-f are momentum slices  
 15 obtained with the beam spot on each of the regions, respectively, along  $\Gamma - \mathbf{K}$  of the  $\text{WSe}_2$  Brillouin  
 16 zone at 100 K (Fig. 2g, inset). As expected, at  $V_G = 0$  (upper row) only the valence bands can be seen.  
 17 Their evolution with layer number is consistent with the literature<sup>27</sup> and matches the overlaid density  
 18 functional theory (DFT) predictions well (Methods). At  $V_G = +3.35 \text{ V}$  (lower row) an additional spot  
 19 appears near  $E_F$ . The size of this conduction band feature is determined solely by the instrument  
 20 resolution. In 1L  $\text{WSe}_2$  the spot is located at  $\mathbf{K}$ , whereas in 2L and 3L it is at  $\mathbf{Q}$  (see Fig. 2g). This is  
 21 consistent with evidence from photoluminescence<sup>25</sup> that the gap is direct at  $\mathbf{K}$  in the monolayer but  
 22 indirect for 2+ layers.



23 **Figure 2. Layer-number dependent conduction band edge (CBE) in  $\text{WSe}_2$ .** (a) Schematic of a device  
 24 incorporating a  $\text{WSe}_2$  flake, with overlapping graphene top contact grounded and gate voltage  $V_G$   
 25 applied to the graphite back gate. (b) Optical and (c) SPEM images of  $\text{WSe}_2$  Device 1 ( $d_{\text{BN}} = 7.4 \pm 0.5$   
 26 nm), with monolayer, bilayer and trilayer regions identified (scale bars, 5  $\mu\text{m}$ ). (d)-(f) Energy-  
 27 momentum slices along  $\Gamma - \mathbf{K}$  for 1L, 2L, and 3L regions respectively. The upper panels are at  $V_G = 0$   
 28 and the lower ones at  $V_G = +3.35 \text{ V}$ . The intensity in the dashed boxes is multiplied by 20. The fuzzy  
 29 spots signal population of the CBE. Scale bars, 0.3  $\text{\AA}^{-1}$ . The data have been reflected about  $\Gamma$  to aid  
 30

1 comparison with DFT predictions (red dashed lines). (g) Brillouin zone of  $\text{MX}_2$ , and schematic of bands  
 2 along  $\Gamma - \text{K}$  showing definitions of the energy parameters discussed in the text.

3 Table 1 displays the band parameters for 1L–3L  $\text{WSe}_2$  as well as for other monolayer  $\text{MX}_2$  species,  
 4 derived<sup>15</sup> from measurements on this and other devices (see SI section S5). The band gap,  $E_g = E_C -$   
 5  $E_K$ , where  $E_C$  is the energy of the CBE, was determined at a doping level of  $n_G \approx 10^{13} \text{ cm}^{-2}$  for which  
 6  $E_F - E_C \sim 30 \text{ meV}$  (see Methods). We also list the simultaneously determined hole effective mass  
 7  $m_K^*$ , valence band edge  $E_K$ , spin-orbit splitting  $\Delta_{\text{SOC}}$ , and  $E_{\text{K}\Gamma}$  as defined in Fig. 2g, all measured for  
 8 the first time on an hBN substrate with no cap and with greater precision than in previous reports.

9

	$\Delta_{\text{SOC}}$ (eV)	$E_K (V_G = 0)$ (eV)	$E_{\text{K}\Gamma} (V_G = 0)$ (eV)	$m_K^*/m_e$	$E_g$ (eV)
1L MoS <sub>2</sub>	$0.17 \pm 0.04$	$1.93 \pm 0.02$	$0.14 \pm 0.04$	$0.7 \pm 0.1$	$2.07 \pm 0.05$
1L MoSe <sub>2</sub>	$0.22 \pm 0.03$	$1.04 \pm 0.02$	$0.48 \pm 0.03$	$0.5 \pm 0.1$	$1.64 \pm 0.05$
1L WS <sub>2</sub>	$0.45 \pm 0.03$	$1.43 \pm 0.02$	$0.39 \pm 0.02$	$0.5 \pm 0.1$	$2.03 \pm 0.05$
1L WSe <sub>2</sub>	$0.485 \pm 0.010$	$0.80 \pm 0.01$	$0.62 \pm 0.01$	$0.42 \pm 0.05$	$1.79 \pm 0.03$
2L WSe <sub>2</sub>	$0.501 \pm 0.010$	$0.75 \pm 0.01$	$0.14 \pm 0.01$	$0.41 \pm 0.05$	$1.51 \pm 0.03^*$
3L WSe <sub>2</sub>	$0.504 \pm 0.010$	$0.74 \pm 0.01$	$0.00 \pm 0.01$	$0.40 \pm 0.05$	$1.46 \pm 0.03^*$

\*indirect, with CBE at  $Q$

10

11

12

13

14

15

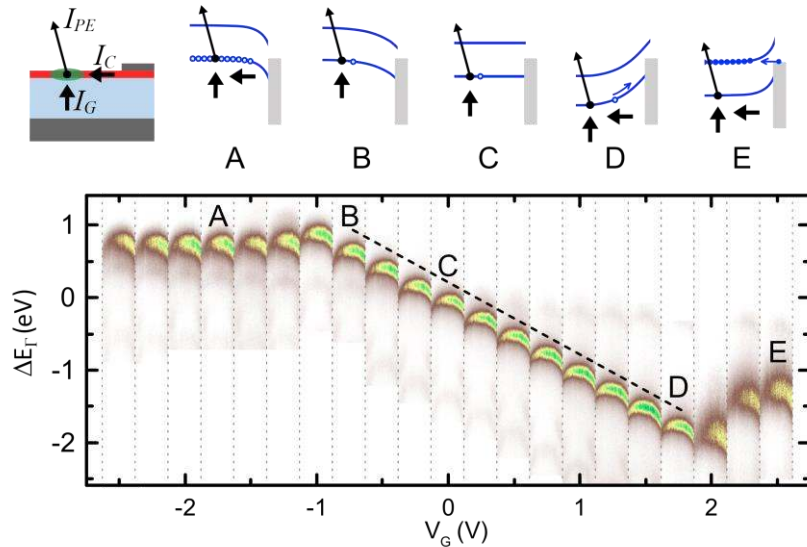
16

17

18

**Table 1. Measured band structure parameters of  $\text{MX}_2$  semiconductors.** As defined in Fig. 2g,  $\Delta_{\text{SOC}}$  is the spin-orbit splitting of the valence band at  $\text{K}$ ;  $E_K$  is the valence band edge at  $V_G = 0$ ;  $E_{\text{K}\Gamma} = E_K - E_\Gamma$  is the difference between the valence band edges at  $\text{K}$  and  $\Gamma$  at  $V_G = 0$ ;  $m_K^*$  is the effective mass of the valence band edge at  $\text{K}$  in units of the free electron mass  $m_e$ ; and  $E_g$  is the band gap measured at gate-induced electron density  $n_G = 1.0 \pm 0.2 \times 10^{12} \text{ cm}^{-2}$ . The stage temperature was 100 K for the  $\text{WSe}_2$  and 105 K for the others.

### 3. Gate dependence of the electronic structure of a semiconducting monolayer



19

20

21

22

23

24

25

26

27

28

29

30

**Figure 3. Electrostatic gating of monolayer  $\text{WSe}_2$ .** Each vertical strip is an energy-momentum slice,  $0.6 \text{ \AA}^{-1}$  wide, through  $\Gamma$  in  $\text{WSe}_2$  Device 2 ( $d_{\text{hBN}} = 6.0 \pm 0.5 \text{ nm}$ ) measured at the gate voltage shown on the bottom axis.  $\Delta E_\Gamma$  is the photoelectron kinetic energy measured relative to the  $\Gamma$ -point maximum at  $V_G = 0$ . The dashed line has slope  $-1/e$ . Above left is a device schematic indicating the photoemission current  $I_{\text{PE}}$  from the beam spot, current  $I_C$  from the graphene contact, and current  $I_G$  from the gate through the BN due to photoconductivity. The schematic band diagrams indicate the situations at the gate voltages labelled A-E. The gray rectangle is the graphene Fermi sea, the blue lines are the  $\text{WSe}_2$  conduction and valence band edges, and the smaller arrows indicate when  $I_G$  and  $I_C$  are significant.

We now investigate the full gate dependence of  $\mu$ -ARPES spectra. Figure 3 shows the behavior of the top of the valence band at  $\Gamma$ , where the photoemission signal is strongest, for monolayer  $\text{WSe}_2$

Device 2. At low  $V_G$  (range labelled B-C-D) the spectrum shifts nearly linearly with a slope  $-1/e$ , where  $e$  is the electron charge, implying that the electrostatic potential in the WSe<sub>2</sub> tracks the gate potential when it is undoped. For  $V_G > +2.1$  V (E) or  $< -1.5$  V (A) it becomes almost independent of  $V_G$ , implying that these are the thresholds for electron and hole accumulation, respectively. The behavior can be understood in more detail with reference to the corresponding band diagrams shown above, taking into account the balance of the current of photoemitted electrons,  $I_{PE}$ , the currents into the beam spot from the contact,  $I_C$ , and the gate,  $I_G$ , as indicated in the sketch at the top left (see Methods).

Note that no change in spectral widths is seen as long as the WSe<sub>2</sub> is insulating (range B-D in Fig. 3), but above threshold (range D-E) all features are smeared in energy by a similar amount. This can be explained by inhomogeneous broadening due to variation of the potential across the beam spot associated with lateral current flow in the WSe<sub>2</sub>. Refinement of the technique to reduce this effect may allow studies of changes in intrinsic broadening with doping.

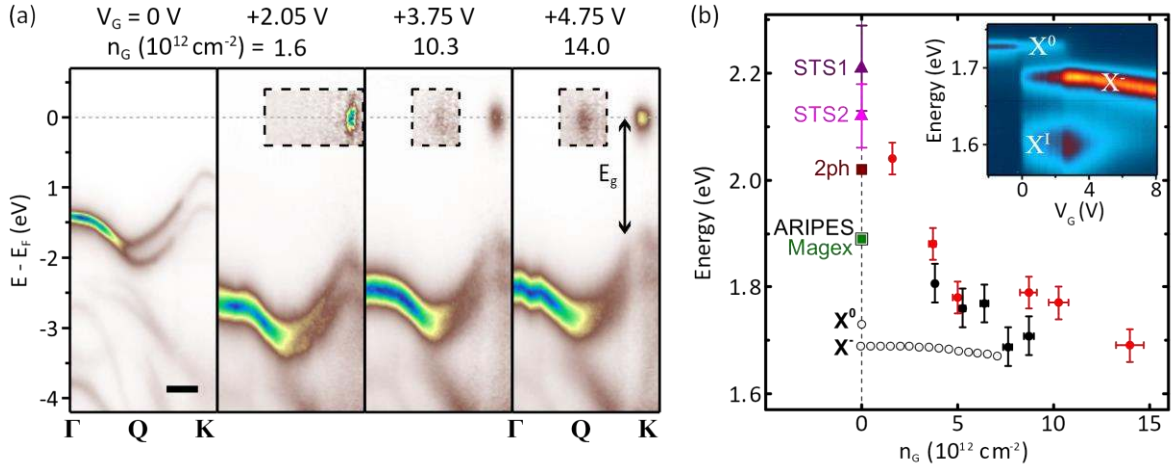


**Figure 4. Renormalization of the band gap and comparison with optical spectroscopy. (a)** Energy-momentum slices along  $\Gamma$ -K for monolayer WSe<sub>2</sub> in Device 1 at a series of  $V_G$ , with doping  $n_G$  also shown (scale bar,  $0.3 \text{ \AA}^{-1}$ ). The intensity in the dashed box is multiplied by 20 at  $+2.05$  V and by 40 at higher  $V_G$ . The definition of the band gap,  $E_g$ , is indicated. **(b)** Band gap dependence on  $n_G$  for Device 1 (red) and also Device 3 ( $d_{BN} = 24.5 \pm 0.5$  nm, solid black circles) at 100 K. Also plotted (black open circles) are the photoluminescence peak positions for the neutral exciton ( $X^0$ ) and negative trion ( $X^-$ ) in Device 3 at the same temperature. The inset shows the photoluminescence data, with an impurity-bound exciton peak  $X^1$  also labelled. The points plotted at  $n_G = 0$  are measurements of the band gap from other techniques taken from the literature: STS1<sup>20</sup> (purple triangle) and STS2<sup>21</sup> (pink triangle) are from scanning tunnelling spectroscopy measurements, on graphite at  $T = 4.5$  K and 77 K respectively; 2ph (brown square) is from two-photon absorption<sup>22</sup>, on SiO<sub>2</sub> at 300 K; ARIPES (black open square) is from inverse photoemission<sup>23</sup>, on sapphire at 300 K; and Magex (green solid square) is from magneto-optical measurements<sup>24</sup>, encapsulated in BN at 4 K.

Figure 4a shows spectra from monolayer WSe<sub>2</sub> Device 1 at  $V_G = 0$  (for reference) and at selected gate voltages well above threshold (about  $+1.5$  V). In this regime we derive the gate doping  $n_G$ , also shown, from the gate capacitance and threshold voltage (see Methods). The CBE becomes visible at **K** for  $n_G > \sim 10^{12} \text{ cm}^{-2}$  and at **Q** for  $n_G > \sim 10^{13} \text{ cm}^{-2}$ , when  $E_K$  is roughly 30 meV below  $E_F$ . We conclude that the conduction band minimum at **Q** is higher than that at **K**. Scanning tunnelling spectroscopy<sup>21</sup> also indicates that for 1L WSe<sub>2</sub> these minima are very close. The form of the valence bands does not change discernibly with increasing  $n_G$ , but they shift upwards in energy while the CBE is pinned at  $E_F$ , implying that the band gap decreases.

Optical spectroscopy can be performed on the same devices, and under the same conditions, as the  $\mu$ -ARPES measurements, eliminating uncertainties due to differences in sample quality, dielectric environment, gate voltage and temperature<sup>28-30</sup>. Figure 4b shows both the  $\mu$ -ARPES determination of  $E_g$  (black solid circles) and the photoluminescence peak positions (black empty circles),  $E_{X^0}$  and  $E_{X^-}$ ,

1 for neutral ( $X^0$ ) and charged ( $X^-$ ) excitons, for monolayer WSe<sub>2</sub> Device 3 as a function of gate doping at  
2 100 K. Also shown are the values of  $E_g$  from Device 1 (red solid circles), which agree to within the  
3 uncertainty. It is apparent that  $E_g$  decreases systematically, by  $\sim 400$  meV, as  $n_G$  rises to  $1.5 \times 10^{13}$   
4  $\text{cm}^{-2}$ . Such renormalization of the band gap with static doping is expected to occur in a semiconductor  
5 as a result of free-carrier screening<sup>31</sup>, though it has not previously been so accessible to experiments.

6 Also plotted in Fig. 4b are values of the band gap at  $n_G = 0$  inferred from several other techniques.  
7 An extrapolation of  $E_g$  measured by  $\mu$ -ARPES to  $n_G = 0$  is consistent with scanning tunneling  
8 spectroscopy (STS) measurements which put it in the range 2.1-2.2 eV. Comparison with  $E_{X^0}$  supports  
9 arguments that the binding energy of neutral excitons in this material is very large<sup>28</sup>, at several  
10 hundred meV.  $E_g$  decreases much faster than  $E_{X^-}$  with doping, implying dramatic weakening of the  
11 exciton binding which is another expected effect of free-carrier screening<sup>29</sup>. Finally, the still smaller  
12 values of  $E_g$  reported in monolayers doped with alkali metals (down to 1.4 eV for 1L WSe<sub>2</sub>) are  
13 consistent with an extrapolation the renormalization process to higher  $n_G$ <sup>7,8</sup>.

14 The ability to measure changes in the electronic bands in 2D field-effect devices opens up many  
15 interesting possibilities. For example, it could be used to study electric-field tuning of the bands across  
16 topological phase transitions<sup>5</sup>; to investigate the doping dependence of spectra in correlated electron  
17 systems such as in superconductors, Mott insulators, and charge-density-wave materials; to observe  
18 spectral reconstructions in structures with moiré superlattice modulations<sup>32</sup>; and, with the addition of  
19 circularly polarized light or a spin-resolved spectrometer, to study electrically controlled magnetic  
20 phenomena<sup>33</sup>.

## 21 22 References

- 23 1. Dudin, P. *et al.* Angle-resolved photoemission spectroscopy and imaging with a submicrometre  
24 probe at the SPECTROMICROSCOPY-3.2L beamline of Elettra. *J. Synchrotron Radiat.* **17**, 445–  
25 450 (2010).
- 26 2. Rotenberg, E. & Bostwick, A. microARPES and nanoARPES at diffraction-limited light sources:  
27 opportunities and performance gains. *J. Synchrotron Radiat.* **21**, 1048–1056 (2014).
- 28 3. Iwasawa, H. *et al.* Buried double CuO chains in YBa<sub>2</sub>Cu<sub>4</sub>O<sub>8</sub> uncovered by nano-ARPES. *J. Phys.*  
29 *Condens. Matter* **4**, 9015–9022 (2019).
- 30 4. Novoselov, K. S., Mishchenko, A., Carvalho, A. & Castro Neto, A. H. 2D materials and van der  
31 Waals heterostructures. *Science*. **353**, aac9439 (2016).
- 32 5. Tong, Q. *et al.* Topological mosaics in moiré superlattices of van der Waals heterobilayers. *Nat.*  
33 *Phys.* **13**, 356–362 (2017).
- 34 6. Bostwick, A., Ohta, T., Seyller, T., Horn, K. & Rotenberg, E. Quasiparticle dynamics in graphene.  
35 *Nat. Phys.* **3**, 36–40 (2007).
- 36 7. Riley, J. M. *et al.* Negative electronic compressibility and tunable spin splitting in WSe<sub>2</sub>. *Nat.*  
37 *Nanotechnol.* **10**, 1043–1047 (2015).
- 38 8. Zhang, Y. *et al.* Electronic Structure, Surface Doping, and Optical Response in Epitaxial WSe<sub>2</sub>  
39 Thin Films. *Nano Lett.* **16**, 2485–2491 (2016).
- 40 9. Kim, J. *et al.* Observation of tunable band gap and anisotropic Dirac semimetal state in black  
41 phosphorus. *Science*. **349**, 723–726 (2015).
- 42 10. Tang, S. *et al.* Quantum spin Hall state in monolayer 1T'-WTe<sub>2</sub>. *Nat. Phys.* **13**, 683–687 (2017).
- 43 11. Koch, R. J. *et al.* Nano focusing of soft X-rays by a new capillary mirror optic. *Synchrotron Radiat.*  
44 *News* **31**, 50–52 (2018).
- 45 12. Zhang, H. *et al.* Resolving Deep Quantum-Well States in Atomically Thin 2H-MoTe<sub>2</sub> Flakes by  
46 Nanospot Angle-Resolved Photoemission Spectroscopy. *Nano Lett.* **18**, 4664–4668 (2018).
- 47 13. Katoch, J. *et al.* Giant spin-splitting and gap renormalization driven by trions in single-layer  
48 WS<sub>2</sub>/h-BN heterostructures. *Nat. Phys.* **14**, 355–359 (2018).
- 49 14. Cucchi, I. *et al.* Microfocus Laser–Angle-Resolved Photoemission on Encapsulated Mono-, Bi-,  
50 and Few-Layer 1T'-WTe<sub>2</sub>. *Nano Lett.* **19**, 554–560 (2019).
- 51 15. Wilson, N. R. *et al.* Determination of band offsets, hybridization, and exciton binding in 2D

- 1 semiconductor heterostructures. *Sci. Adv.* **3**, e1601832 (2017).
- 2 16. Jin, W. *et al.* Tuning the electronic structure of monolayer graphene/ MoS<sub>2</sub> van der Waals  
3 heterostructures via interlayer twist. *Phys. Rev. B* **92**, 201409 (2015).
- 4 17. Pierucci, D. *et al.* Band Alignment and Minigaps in Monolayer MoS<sub>2</sub>-Graphene van der Waals  
5 Heterostructures. *Nano Lett.* **16**, 4054–4061 (2016).
- 6 18. Liu, Y. *et al.* Van der Waals heterostructures and devices. *Nature Reviews Materials* **1**, 16042  
7 (2016).
- 8 19. Schaibley, J. R. *et al.* Valleytronics in 2D materials. *Nat. Rev. Mater.* **1**, 16055 (2016).
- 9 20. Yankowitz, M., McKenzie, D. & LeRoy, B. J. Local Spectroscopic Characterization of Spin and  
10 Layer Polarization in WSe<sub>2</sub>. *Phys. Rev. Lett.* **115**, 136803 (2015).
- 11 21. Zhang, C. *et al.* Probing Critical Point Energies of Transition Metal Dichalcogenides: Surprising  
12 Indirect Gap of Single Layer WSe<sub>2</sub>. *Nano Lett.* **15**, 6494–6500 (2015).
- 13 22. He, K. *et al.* Tightly Bound Excitons in Monolayer WSe<sub>2</sub>. *Phys. Rev. Lett.* **113**, 026803 (2014).
- 14 23. Park, S. *et al.* Direct determination of monolayer MoS<sub>2</sub> and WSe<sub>2</sub> exciton binding energies on  
15 insulating and metallic substrates. *2D Mater.* **5**, 025003 (2018).
- 16 24. Stier, A. V. *et al.* Magneto-optics of exciton Rydberg states in a monolayer semiconductor. *Phys.*  
17 *Rev. Lett.* **120**, 057405 (2018).
- 18 25. Zhao, W., Ribeiro, R. M. & Eda, G. Electronic Structure and Optical Signatures of  
19 Semiconducting Transition Metal Dichalcogenide Nanosheets. *Acc. Chem. Res.* **48**, 91–99  
20 (2015).
- 21 26. Mayorov, A. S. *et al.* Micrometer-Scale Ballistic Transport in Encapsulated Graphene at Room  
22 Temperature. *Nano Lett.* **11**, 2396–2399 (2011).
- 23 27. Liu, G., Xiao, D., Yao, Y., Xu, X. & Yao, W. Electronic structures and theoretical modelling of two-  
24 dimensional group-VIB transition metal dichalcogenides. *Chem. Soc. Rev.* **44**, 2643–2663  
25 (2015).
- 26 28. Ugeda, M. M. *et al.* Giant bandgap renormalization and excitonic effects in a monolayer  
27 transition metal dichalcogenide semiconductor. *Nat. Mater.* **13**, 1091–1095 (2014).
- 28 29. Gao, S., Liang, Y., Spataru, C. D. & Yang, L. Dynamical Excitonic Effects in Doped Two-  
29 Dimensional Semiconductors. *Nano Lett.* **16**, 5568–5573 (2016).
- 30 30. Raja, A. *et al.* Coulomb engineering of the bandgap and excitons in two-dimensional materials.  
31 *Nat. Commun.* **8**, 15251 (2017).
- 32 31. Gao, S. & Yang, L. Renormalization of the quasiparticle band gap in doped two-dimensional  
33 materials from many-body calculations. *Phys. Rev. B* **96**, 155410 (2017).
- 34 32. Cao, Y. *et al.* Magic-angle graphene superlattices: a new platform for unconventional  
35 superconductivity. *Nature* **556**, 43–50 (2018).
- 36 33. Wang, H., Fan, F., Zhu, S. & Wu, H. Doping enhanced ferromagnetism and induced half-  
37 metallicity in CrI<sub>3</sub> monolayer. *EPL* **114**, 47001 (2016).
- 38

### 39 Acknowledgements.

40 The Engineering and Physical Sciences Research Council is acknowledged for support through  
41 EP/P01139X/1 and a studentship for NCT (EP/M508184/1). XXia was supported by a University of  
42 Warwick studentship. DHC and PVN were supported by US Department of Energy, Office of Basic  
43 Energy Sciences, Division of Materials Sciences and Engineering, award DE-SC0002197 and the Pro-  
44 QM Energy Frontiers Research Center. PVN and JK were also supported in part by NSF MRSEC award  
45 1719797. XXu and NPW are supported by Department of Energy, Basic Energy Sciences, Materials  
46 Sciences and Engineering Division (DE-SC0018171). NDMH and GCC acknowledge the support of the  
47 Winton Programme for the Physics of Sustainability. Computing resources were provided by the  
48 Darwin Supercomputer of the University of Cambridge High Performance Computing Service. GCC  
49 acknowledges the support of the Cambridge Trust European Scholarship.

50



## 1 Author contributions.

2 NRW, XXu and DHC conceived and supervised the project. PVN, JK and NW fabricated the samples.  
3 NCT, NRW, PVN, XXia, AJG, VK, AG and AB collected  $\mu$ -ARPES data. NCT, NRW and PVN analyzed  $\mu$ -  
4 ARPES data, with input from AB. NPW acquired photoluminescence data. NDMH, NY and GCC  
5 performed the band structure calculations. DHC, NRW, PVN and XXu wrote the paper with input from  
6 all authors.  
7

## 8 Competing interests.

9 The authors declare no competing interests.  
10

## 11 Materials & Correspondence.

12 Correspondence to cobden@uw.edu, xuxd@uw.edu, neil.wilson@warwick.ac.uk  
13

## 14 Methods

15 **Sample fabrication.** Standard micro-mechanical exfoliation and dry transfer<sup>34</sup> with polycarbonate  
16 film-based stamping were used. The smaller electrode contacts the graphite gate, as indicated in the  
17 optical micrograph in Fig. 1c. The larger electrode, which contacts the graphene, is grounded and  
18 covers most of the chip to minimize electrostatic distortion of the photoelectron spectrum when  
19 applying a gate voltage. The sample substrates are mounted in dual-inline packages using ultra-high  
20 vacuum and high-temperature compatible silver epoxy and wire-bonded. Bare wire is wrapped around  
21 the package pins, fixed using the epoxy, and used to contact to leads on the ARPES sample mount.

22 **Angle resolved photoemission.** Measurements were made at the Spectromicroscopy beamline of  
23 the Elettra light source<sup>1</sup>. Linearly polarized light, at 45° to the sample, was focused to a  $\sim 0.6$   $\mu\text{m}$   
24 diameter spot by a Schwarzschild objective. The photon energy was 27 eV except for the data in Fig.  
25 1 where it was 74 eV. The hemispherical analyser with two-dimensional detector on a two-axis  
26 goniometer permitted a resolution of approximately 50 meV and 0.03  $\text{\AA}^{-1}$ . After mounting in the  
27 chamber on a scanning stage with 100 nm closed loop positioning accuracy, the samples were located  
28 by scanning photoemission microscopy (SPEM). With the light focus fixed, the photoelectron intensity  
29 on the detector was acquired point by point as the sample was stepped relative to the light spot. In  
30 the SPEM images the colour corresponds to the integrated photoelectron intensity around  $\Gamma$  (over the  
31 full detector range of  $\sim 15^\circ$ , corresponding to  $\sim 0.6$   $\text{\AA}^{-1}$  at 20 eV and  $\sim 1.1$   $\text{\AA}^{-1}$  at 70 eV, and binding  
32 energy range of 0 to 2.5 eV in Fig. 1d and 0 to 3.5 eV in Fig. 2c) at that point on the sample. For spectral  
33 acquisition, the entrance slit to the analyser is in a fixed orientation, but its angular coordinates  
34 relative to the sample normal are controlled by the two-axis goniometer. For energy-momentum slices  
35 along  $\Gamma - \mathbf{K}$ , as in Figs. 2 and 3, a sequence of 2D slices was acquired with the goniometer moving the  
36 centre of the analyser entrance slit along the line in reciprocal space from  $\Gamma - \mathbf{K}$ , mapping out a small  
37 volume in  $(E, k_x, k_y)$  from which the  $\Gamma - \mathbf{K}$  slice was later extracted. Over the few hours required to  
38 acquire this data, the sample drift was typically  $< 1$   $\mu\text{m}$ . Prior to measurement, samples were annealed  
39 in ultrahigh vacuum at 650 K for several hours. The stage temperature was  $\sim 100$  K (Figs. 2,3 and 4) or  
40  $\sim 105$  K (Fig. 1 and MoS<sub>2</sub>, WS<sub>2</sub> and MoSe<sub>2</sub>). Following standard practice, we plot  $E - E_F$ , the negative  
41 of the electron binding energy, where  $E$  is the measured photoelectron kinetic energy and  $E_F$  is the  
42 kinetic energy of electrons removed from the Fermi level, determined by fitting the Fermi-Dirac  
43 distribution to the drop in photoemitted intensity across the photoemission threshold.

44 **Detailed considerations of gate dependence and device operation.** The devices have a thin hBN  
45 dielectric separating the graphite back-gate electrode from the upper 2D material (2DM) layer, which  
46 is either graphene itself or overlaps a graphene contact that in turn overlaps a metal (ground)  
47 electrode. When the 2DM is conducting this constitutes a parallel-plate capacitor with geometric areal  
48 capacitance  $C_g = \epsilon_0 \epsilon_{BN} / d_{BN}$ , where  $\epsilon_0$  is the relative permittivity of free space,  $\epsilon_{BN} = 4.0 \pm 0.2$  is  
49 the out-of-plane (c direction) dielectric constant for hBN, and  $d_{BN}$  is the thickness of the hBN. During  
50 photoemission, the electrochemical potential at the emission spot will differ from ground, by an  
51 amount  $\Delta V$ , associated with current flow both to the contact and to the gate which is at voltage  $V_g$ ,

1 thus reducing the effective gate voltage determining the local carrier density to  $V_g - \Delta V$ .  $\Delta V$  will not  
 2 exceed the product of the effective electrical resistance  $R$  between the spot and ground electrode  
 3 and the maximum current, which is no more than  $\sim 2$  nA.

4 For **graphene devices**, the band dispersion is not affected by doping to within 10% accuracy (see  
 5 Extended Data Fig. 4). In this case we expect  $n_G = C_g(V_G - \Delta V - \Delta\mu/e)$ , where  $\Delta\mu = \Delta(E_F - E_D)$  is  
 6 the chemical potential change due to gate doping (note that  $C_g$  is only the geometric capacitance, and  
 7 the total capacitance is nonlinear in  $V_G$ ). For graphene,  $R < \sim 1$  k $\Omega$  and thus  $\Delta V < \sim 2$   $\mu$ V, which is  
 8 negligible.  $\Delta\mu$  can be found from the ARPES spectrum at each gate voltage to an accuracy of  $\sim 20$  meV.  
 9 In the measurements shown in Fig. 1,  $\Delta\mu/e$  is at least ten times smaller than  $V_G$ , and thus simply taking  
 10  $n_G \approx C_g V_G$ , the quantity plotted on the top axis of Fig. 1f, is accurate to  $< 10\%$ . When  $k_B T \ll E_D$  (valid  
 11 here since  $k_B T = 9$  meV), from the conical Dirac dispersion one expects<sup>35</sup>  $E_D^2 \approx \pi \hbar^2 v_F^2 (n_0 + n_G)$ ,  
 12 where  $n_G = C V_G$  is the gate-induced 2D electron density,  $C$  the areal capacitance, and  $n_0$  the residual  
 13 electron density at  $V_G = 0$ . The solid line in Fig. 1f is a fit to this model with  $C$  and  $n_0$  treated as fitting  
 14 parameters. The value of  $n_0$  obtained is  $(1.8 \pm 0.1) \times 10^{12}$  cm $^{-2}$ , implying a somewhat high residual  
 15 doping that may be due to contamination. The value of  $C$  is  $(2.2 \pm 0.2) \times 10^{-7}$  Farad cm $^{-2}$ , consistent  
 16 with the geometrical capacitance,  $\frac{\epsilon_0 \epsilon_{BN}}{d_{BN}} = (2.5 \pm 0.2) \times 10^{-7}$  Farad cm $^{-2}$ , derived from the BN  
 17 thickness,  $d_{BN} = 14 \pm 1$  nm, measured by atomic force microscopy, and the dielectric constant,  
 18  $\epsilon_{BN} = 4.0$ , taken from the literature<sup>36–38</sup>. Note also that the intensity near  $E_D$  is weak because these  
 19  $E - k$  slices do not pass exactly through  $\mathbf{K}$ . The much lower intensity on one side of the cone results  
 20 from destructive interference between the two carbon sublattices<sup>39</sup>.

21 For **MX<sub>2</sub> semiconductor devices** the situation is more complicated. At small  $V_G$ , the doping  $n_G$  must  
 22 be very small because of the band gap, so the in-plane resistance can be large and  $\Delta V$  can be  
 23 substantial. As long as  $n_G$  is negligible the bands will not be renormalized and  $\Delta V$  can be identified  
 24 with the purely electrostatic energy shift of an ARPES spectral feature.  $\Delta E_\Gamma/e$  in Fig. 3 indeed tracks  
 25  $V_G$  closely at low  $V_G$  (see Extended Data Fig. 6). We deduce that in this regime photoemission directly  
 26 from the hBN valence band generates conductivity in the hBN which is sufficient to keep the potential  
 27 in the MX<sub>2</sub> close to that of the gate, i.e.,  $\Delta V \approx V_g$ , with negligible potential drop across the hBN and  
 28 no accumulation of charge in the MX<sub>2</sub>. In contrast, at a sufficiently large magnitude of  $V_G$ ,  
 29  $(V_G - \Delta E_\Gamma/e)$  tends towards a linear increase with  $V_G$ . This happens when the high doping makes in-  
 30 plane resistance  $R$  small enough that the electrochemical potential in the MX<sub>2</sub> approaches that in the  
 31 (ground) electrode and  $\Delta V$  stops changing, with the Fermi energy virtually pinned at the band edge  
 32 due to the large density of states. In this regime we can take  $n_G = C_g(V_G - \Delta E_\Gamma/e)$ , since  $V_G - \Delta E_\Gamma/e$   
 33 is the static potential drop across the hBN, the electrons are in electrochemical equilibrium, and the  
 34 quantum capacitance is negligible (i.e.,  $E_F$  is effectively pinned at the CBE). The values of  $n_G$  shown in  
 35 Fig. 4 are obtained in this way.

36 Our interpretation of the behavior in Fig. 3 for monolayer WSe<sub>2</sub> is as follows. The photoemission  
 37 current  $I_{PE}$ , current to the contact,  $I_C$ , and to the gate,  $I_G$ , indicated in the sketch at the top left of Fig.  
 38 3, must sum to zero.  $I_G$  can be substantial because of photo-excited carriers in the BN. (It should be  
 39 borne in mind that in general such currents may cause a device to operate differently from how it  
 40 would in the dark). Between B and C, the WSe<sub>2</sub> is depleted and insulating enough that the BN  
 41 photoconductivity brings the potential close to that of the gate. Holes created by photoemission from  
 42 the WSe<sub>2</sub> recombine with excited electrons in the BN, and  $I_{PE} \approx I_G$ . Between C and D, these holes can  
 43 also drift to the contact through the depleted WSe<sub>2</sub>, and  $I_C$  is significant. Above threshold, at E,  
 44 electrons accumulate at the CBE in the WSe<sub>2</sub> as they flow in laterally from the graphene contact, and  
 45 the CBE is pinned close to the graphene Fermi level. Similarly, at A, holes accumulate and the valence  
 46 band edge is pinned. An “overshoot” occurs at D because when the CBE in the beam spot first moves  
 47 below the graphene Fermi level, the Schottky barrier between graphene and WSe<sub>2</sub> prevents electrons  
 48 flowing in fast enough to accumulate.

49 **Estimating the CBE energy.** The structure of the conduction band is not resolvable in the ARPES  
 50 data (Fig. 2d-f). The density of states at a single parabolic band edge is  $g_{2D} = g_s g_v m^* / \hbar^2$ , with spin  
 51 and valley degeneracies  $g_s$  and  $g_v$  and effective mass  $m^*$ . For 1L WSe<sub>2</sub> the conduction band edges are

1 at the K-points, so  $g_v = 2$ , and the band is spin-split by  $\approx 40$  meV<sup>40</sup>, hence  $g_s = 1$  for moderate  
2 doping. Calculations<sup>40</sup> give  $m^* \approx 0.3m_e$ . Using  $n_G = \int_{E_C}^{\infty} F(E)g_{2D} dE$ , where  $F(E)$  is the Fermi-Dirac  
3 distribution, then gives  $E_F - E_C \approx 30$  meV at  $n_G = 1.0 \times 10^{13}$  cm<sup>-2</sup>.

4 **Optical spectroscopy.** Photoluminescence measurements were performed using  $\sim 20$   $\mu$ W linearly  
5 polarized 532 nm continuous-wave laser excitation in reflection geometry, with the signal collected  
6 by a spectrometer and a silicon charge-coupled device, in vacuum in a closed-cycle cryostat.

7 **Electronic structure calculations** including spin-orbit interaction were made using the Quantum  
8 Espresso DFT package<sup>41</sup>. Structures were first optimized until forces were smaller than  $10^{-4}$  Ry / Bohr.  
9 Geometry optimisations and band structure calculations were performed with an  $18 \times 18$  in-plane k-  
10 point grid with 140 Ry plane-wave energy cut off. To avoid interaction between periodic images, the  
11 vacuum spacing was 25.0 Å. We used norm-conserving fully relativistic pseudopotentials<sup>42</sup> from  
12 PseudoDojo<sup>43</sup>, where the semi-core 4d, 5s and 5p states for W are retained as valence electrons. This  
13 results in a lattice constant of 3.32 Å for all three structures. We used the results from calculations  
14 with the PBE functional as a starting point for  $G_0W_0$  calculations which utilised the Yambo code<sup>44</sup>, with  
15 the Godby–Needs plasmon pole approximation<sup>45</sup>. We used 300 bands, 500 bands and 700 bands for  
16 the mono-layer, bilayer and trilayer  $WSe_2$ , respectively, for the self-energy and dynamical dielectric  
17 screening. In order to treat the divergence of the Coulomb interaction during the self-energy  
18 calculation, the random integration method<sup>46</sup> was used, with  $3 \times 10^6$  random q-points and 100 random  
19 G vectors.

20 **Data availability.** All data presented in this paper are available at [to be finalised on acceptance].  
21 Additional data related to this paper may be requested from the authors.

- 22
- 23 34. Zomer, P. J., Guimarães, M. H. D., Brant, J. C., Tombros, N. & Van Wees, B. J. Fast pick up  
24 technique for high quality heterostructures of bilayer graphene and hexagonal boron nitride.  
25 *Appl. Phys. Lett.* **105**, 013101 (2014).
- 26 35. Fang, T., Konar, A., Xing, H. & Jena, D. Carrier statistics and quantum capacitance of graphene  
27 sheets and ribbons. *Appl. Phys. Lett.* **91**, 092109 (2007).
- 28 36. Yu, G. L. *et al.* Interaction phenomena in graphene seen through quantum capacitance. *Proc.*  
29 *Natl. Acad. Sci.* **110**, 3282–3286 (2013).
- 30 37. Dean, C. R. *et al.* Boron nitride substrates for high-quality graphene electronics. *Nat.*  
31 *Nanotechnol.* **5**, 722–726 (2010).
- 32 38. Kim, K. K. *et al.* Synthesis and Characterization of Hexagonal Boron Nitride Film as a Dielectric  
33 Layer for Graphene Devices. *ACS Nano* **6**, 8583–8590 (2012).
- 34 39. Mucha-Kruczyński, M. *et al.* Characterization of graphene through anisotropy of constant-  
35 energy maps in angle-resolved photoemission. *Phys. Rev. B* **77**, 195403 (2008).
- 36 40. Kormányos, A. *et al.* k · p theory for two-dimensional transition metal dichalcogenide  
37 semiconductors. *2D Mater.* **2**, 022001 (2015).
- 38 41. Giannozzi, P. *et al.* QUANTUM ESPRESSO: a modular and open-source software project for  
39 quantum simulations of materials. *J. Phys. Condens. Matter* **21**, 395502 (2009).
- 40 42. Hamann, D. R. Optimized norm-conserving Vanderbilt pseudopotentials. *Phys. Rev. B -*  
41 *Condens. Matter Mater. Phys.* **88**, 085117 (2013).
- 42 43. van Setten, M. J. *et al.* The PSEUDODOJO: Training and grading a 85 element optimized norm-  
43 conserving pseudopotential table. *Comput. Phys. Commun.* **226**, 39–54 (2018).
- 44 44. Marini, A., Hogan, C., Grüning, M. & Varsano, D. yambo: An ab initio tool for excited state  
45 calculations. *Comput. Phys. Commun.* **180**, 1392–1403 (2009).
- 46 45. Godby, R. W. & Needs, R. J. Metal-insulator transition in Kohn-Sham theory and quasiparticle  
47 theory. *Phys. Rev. Lett.* **62**, 1169–1172 (1989).
- 48 46. Castro, A., Räsänen, E. & Rozzi, C. A. Exact Coulomb cutoff technique for supercell calculations  
49 in two dimensions. *Phys. Rev. B - Condens. Matter Mater. Phys.* **80**, 033102 (2009).